

January 01, 2011

Magnetic and magnetotransport characteristics of nanostructures and nanostructured semiconductor systems

Steven Bennett
Northeastern University

Recommended Citation

Bennett, Steven, "Magnetic and magnetotransport characteristics of nanostructures and nanostructured semiconductor systems" (2011). *Mechanical Engineering Master's Theses*. Paper 52. <http://hdl.handle.net/2047/d20002412>

This work is available open access, hosted by Northeastern University.

Magnetic and Magnetotransport Characteristics of Nanostructures and Nanostructured Semiconductor Systems

A Thesis Presented

by

Steven Bennett

to

The Department of Mechanical Engineering

In partial fulfillment of the requirements

for the degree of

Masters of Science

in

Mechanical Engineering

In the field of

Materials Engineering

Northeastern University
Boston, Massachusetts

December, 2011

ABSTRACT

The unique properties of single domain magnetic nanoparticles have been studied since the 1950's.⁴ When a material is geometrically confined to nanoscale dimensions its characteristic properties can change dramatically. In this thesis the magnetic and magnetotransport characteristics of GaMnAs and MnAs nanostructured systems are explored in several novel experimental studies. The ternary magnetic semiconductor GaMnAs was investigated under 3 dimensions (3D) of spatial confinement.¹ Up until this research, GaMnAs hadn't been successfully fabricated, or studied, as a nanodot. By creating a novel patterning approach using anodic porous alumina, the superparamagnetism of confined GaMnAs was able to be acquired using SQUID magnetometry. I also studied GaAs crystalline nanocomposites fabricated with dispersed MnAs nanoparticles.² The embedded nanoparticles created a disordered electronic structure displaying a linear-in-H magnetoresistance up to very high fields (14 T). Through further thermomagnetic characterization studies and data analyses, a fascinating relation was realized. It turned out that a non-saturating linear magnetoresistance is governed strictly by the average macroscopic carrier mobility and not carrier concentration. This is a very important observation, for it realizes a universal model for the nature of linear magnetoresistance phenomena in disordered crystalline materials. Finally, we developed a non-invasive method to quantify the size distribution of nanoparticles in the GaAs matrix.³ This numerical method makes use of thermomagnetic measurements from SQUID magnetometry to generate a plot for the distribution probability vs. particle diameter. Implementation on the MnAs-GaAs samples resulted in a log normal distribution of superparamagnetic particles through the matrix. Overall, this thesis outlines studies that make definitive steps forward in our understanding of the superparamagnetism of magnetic nanodots, magnetotransport in linear magnetoresistive nano-composite systems and the quantified calculation of a composite thin films nanoparticle size distribution.

Preface

This thesis is a summary of studies that I worked on in Dr. Don Heiman's nanoscale semiconductor research laboratory in the Egan research center at Northeastern University. The first study, "*Magnetic Properties of GaMnAs Nanodot Arrays Fabricated using Porous Alumina Templates*"¹, was performed in collaboration with Dr. Latika Menon's nanophysics lab. The second and third studies, "*Universal properties of linear magnetoresistance in strongly disordered MnAs-GaAs composite semiconductors*"², and "*Determining magnetic nanoparticle size distributions from thermomagnetic measurements*"³ were in collaboration with Dr. Laura H. Lewis in the Chemical Engineering Department.

Steve Bennett, 2011

ACKNOWLEDGMENTS

I am deeply indebted to my advisor and mentor Dr. Don Heiman. Without his constant guidance, support and good nature, I would never have been able to achieve a higher level of education in nanoscience and solid state physics; there are not enough words to describe how his passion and patience has inspired me over the years.

I thank Dr. Teiichi Ando for his periodic inspirational words and academic guidance.

I must also express my sincere thanks and appreciation to Dr. Latika Menon for her unending support, research direction and creative insight. Also a sincere thanks to Dr. Laura H. Lewis for lending last minute support when I thought all was lost. In a similar facet I thank Dr. Moneesh Upmanyu, Welville Nowak and Dr. Vince Harris for guidance during my Masters studies.

I thank my colleagues, for their direct contribution to the work, Robert DiPietro, Thomas Nummy, Rhadika Barua, Hannah Johnson, William Fowle and Tim Hussey.

I thank my family for their unwavering encouragement and years of undying support.

Most of all I thank my loving partner Andrea, without whom none of this would have ever been possible.

Contents

- **Abstract**, pg.2
- **Preface**, pg.3
- **Acknowledgements**, pg.4
- **Table of Contents**, pg.5
- **Introduction**, pg.6
- **I: Magnetic properties of GaMnAs nanodot arrays fabricated using porous alumina templates¹**, pg. 8
 - Background, pg. 9
 - Experimental, pg. 11
 - Results, pg. 14
 - Conclusions, pg. 16
- **II: Universal properties of linear magnetoresistance in strongly disordered MnAs-GaAs composite semiconductors²**, pg. 17
 - Background, pg. 18
 - Experimental, pg. 19
 - Results, pg. 22
 - Discussion, pg. 25
 - Conclusions, pg. 27
- **III: Determining magnetic nanoparticle size distributions from thermomagnetic measurements³**, pg. 28
 - Background, pg. 29
 - Methods, pg. 29
 - Experimental Application, pg. 31
 - Conclusions, pg. 36
- **Bibliography**: pg. 37

INTRODUCTION:

The unique properties of single domain magnetic nanoparticles have been studied since the 1950's.⁴ When a material is geometrically confined to nanoscale dimensions its characteristic properties can change dramatically. For instance, when a semiconductor is confined in 3 dimensions to sizes approaching and smaller than its own exciton-bohr radius, its band structure can be radically altered. A spherical semiconductor materials radius can be tuned to luminescence at a precise engineered wavelength.⁵ These nanodots have since been widely used for medical research replacing dyes because of their high stability and improved luminescence characteristics. Ferromagnetic metal nanostructures have been found to be especially fascinating, showing their potential applications in high-density data storage.⁶ Other possible applications rely on their collective magnetic characteristics when distributed in a highly-ordered two-dimensional (2D) matrix, or when dispersed within the crystal structure of a host lattice.^{7,8}

This thesis's sections outline my work in nanomagnetism. These investigations make definitive steps forward in our understanding of the superparamagnetism of magnetic nanodots, magnetotransport in linear magnetoresistive nano-composite systems and the quantification of nanoparticle size distribution solely from thermomagnetic data.

Up until this research, GaMnAs hadn't been successfully fabricated, or studied, in its 3 dimensionally (3D) confined state. This is because the typical fabrication techniques employed in the synthesis of these structures are not applicable to this material. As of the date of the study, resolution limits of EBL (electron beam lithography) ruled it out as a possible patterning technique. The other method often used to create superparamagnetic nanodots is self-assembly, but for the GaMnAs system low growth temperatures restrict the mobility to levels too low for this to occur. At any temperature higher than 200 °C the Mn in the film will coalesce and form Mn rich nano-islands, effectively removing it from the GaAs matrix. For these reasons a novel fabrication method had to be devised to create the GaMnAs structures necessary for studying the material in its geometrically confined form. This also marked the first time that this technique had been used to create nano-disks of an epitaxially grown thin film.

I also investigated GaAs crystalline matrices fabricated with dispersed MnAs nanoparticles via self assembly. The embedded nanoparticles created a disordered electronic structure that displayed a linear-in-H magnetoresistance up to very high fields (14 T). Through further thermomagnetic characterization studies and data analyses, a fascinating relation was realized. We discovered that

the non-saturating linear magnetoresistance is governed strictly by the average macroscopic carrier mobility. This macroscopic carrier mobility, in this case, is altered primarily by the incorporation of these MnAs nanodots. This is a very important observation, for it realizes a universal model for the nature of linear magnetoresistance phenomena in disordered crystalline materials.

Finally, my work on the MnAs-GaAs system spawned another advancement. In order to fully understand our samples so as to create an accurate model for its linear magnetoresistive behavior, we needed to investigate the size distribution of the nanoparticles throughout the thin film. To do this, we developed a novel method which relies only on thermomagnetic measurements to calculate a log-normal curve for the distribution of particle diameters in the sample. This numeric method marks the first time that the distribution probability as a function of particle diameter had been successfully obtained, and verified, using zero-field-cooled magnetic data obtained via SQUID magnetometry. This study not only helps solidify understanding of the structure of the systems and how it influences the linear magnetoresistance effect, but it also proposes a new technique for characterizing any system of dispersed single domain superparamagnetic nanoparticles.

1. Magnetic properties of GaMnAs nanodot arrays fabricated using porous alumina templates¹

Nanotechnology and the study of materials on the nanoscale has grown to question what unique properties some materials may have when confined in nanoscale geometries. Fabrication of highly-ordered nanodot arrays composed of quantum dot semiconductors⁹ and ferromagnetic nanoparticles^{10,11,12} is at the forefront of materials science as advanced devices call for smaller nanostructured systems¹³. It's already known that semiconductor materials can be fabricated in dimensions approaching and sometimes undercutting their own exciton Bohr radius. The exciton Bohr radius is the radial distance that an orbiting electron moves. This dimension can also be understood as the distance between an electron and its associated hole. When a semiconductor material is confined to dimensions approaching or smaller than this dimension its binding energy is increased due to quantum confinement, first found by *A.I. Ekimov et. al*¹⁴ in 1982. The state of quantum confinement is already known to drastically change a material's inherent properties. This effect is especially useful for tuning the wavelength of the photoluminescence. By controlling precisely the dimensions of the confined quantum dot one can, in essence, control the band gap of the material. This will change the wavelength of the emitted photon from an electron excitation. Size-dependent photoluminescence is the most widely used property of nanoscale confinement, but another important aspect is the variation of magnetic characteristics with dimensional confinement. A material, such as the Dilute Magnetic Semiconductor (DMS) GaMnAs, can undergo a shift in magnetic state when confined beyond a point call the superparamagnetic limit. This is currently a hot topic in chip manufacture and nanoelectronics for memory applications. This limit presents as a barrier to the limiting size for magnetic devices. The reason for this is that once the size is shrunk beyond this point the magnetic moment of a material can be affected simply by temperature fluctuations. This has presented a huge hurdle to the memory and computing industry, forcing advances to develop new device technologies that don't rely on the material's characteristics that are obstructed by confinement.

Most applications for a magnetic material in a memory device are centered on their ferromagnetism. When the material is confined sufficiently to be superparamagnetic it will no longer exhibit the spontaneous magnetism that is synonymous with a ferromagnetic material. Its spin orientation can flip randomly under the influence of temperature. Though random, there is an average amount of time between flips and is referred to as the Neel relaxation time. When the amount of time used to characterize the magnetic moment of the material is larger than the Neel relaxation time, it can

appear that the material has no net magnetization. Even though it has no net magnetization an external field can magnetize the particles in a specific direction, similar to a paramagnetic material, but with a moment much larger than that of a single ion. This is why one must compare a zero-field-cooled (ZFC) to a field-cooled (FC) curve to characterize superparamagnetism in nanostructures. This gives an idea of the thermal effects on the spin with and without external orientation manipulation.

BACKGROUND:

GaMnAs is a dilute magnetic semiconductor (DMS). Its structure is that of GaAs (zincblende crystal) with Mn ions at Ga substitutional positions. This crystal structure exhibits ferromagnetism, making GaMnAs a significant material for spintronics applications, (seeing as it is also a semiconductor). Its unique ferromagnetism arises from hole-mediated ferromagnetic ordering that produces its spontaneous magnetic state¹⁵. There is an antiferromagnetic p-d exchange (hole-ion) between the valence band hole (spin moment 3/2) and Mn (spin moment 3/2), resulting in an overall spin moment of $j = 1$. Working together with GaAs, GaMnAs has a lot of promise as a candidate for spintronic devices and spin filter functionality. In order to make such applications viable, full understanding of the materials properties in confined geometries is vital. This indirect hole-mediated ferromagnetism inherent in DMS is not a result of the valence structure itself, but of the special characteristics of the Mn acceptors.

It is expected that when GaMnAs is under quantum confinement it will exhibit superparamagnetism rather than ferromagnetism. As of the date of our study, though, this has not been verified due to fabrication constraints. Thin film deposition can easily be calibrated to allow for deposition of GaMnAs to within angstroms of anything larger than $\sim 2\text{nm}$, but methods of in-plane stereolithographic patterning cannot obtain the sizes necessary to confine GaMnAs in the remaining two dimensions. Therefore in order to create small enough structures to study this DMS within these constraints another technique must be investigated.

Research into the properties of ordered nanodot arrays of confined nanostructures currently relies on self-assembly and lithography. The downsides of lithography are the speed at which production can take place and the limitations on the minimum size of structures. Alternatively, a downside to self-assembly is that not all materials will simply self-assemble into nanostructures on mismatched substrates. It has been shown that when a material is grown on a lattice mismatched

substrate it may form into quantum dots, but this is only inherent in some material systems and at specific temperatures (particle motilities). It depends largely on material-dependent factors such as the contact angle of the molten dot once it contacts the surface and the degree of lattice mismatch between the deposited materials and the substrate. Self-assembly also lacks the high degree of order that is needed for many applications such as memory devices and photonic crystals. One other promising technique that is currently being investigated is the use of porous templates such as anodic porous alumina. These templates can be fabricated with a high degree of order and the pore sizes can be tuned to specific dimensions. They have been used as shadow masks for direct deposition through the material onto a substrate,^{16,17,18} selective etching of an underlying film,^{19,20} and the preparation of imprint molds by etching onto an underlying substrate^{21,22,23}.

To the date of this study, the properties of GaMnAs in its 3D confined state had not been investigated. Synthesizing this ternary dilute magnetic semiconductor as a quantum dot had proved to be a significant challenge. Similar semiconductor materials such as InAs will self-assemble into nanodots when grown on a lattice mismatched substrate (GaAs 111). But to do this a temperature high enough to introduce sufficient mobility for such an evolution to occur must be achieved. Like most other binary and ternary semiconductors GaMnAs does not maintain its crystalline state if grown on a lattice mismatched substrate at high enough temperatures for self assembly to occur. Introduction of high mobility Mn into the GaAs lattice requires low substrate growth temperatures ($T \sim 200\text{-}250\text{ }^\circ\text{C}$). Otherwise the Mn atoms move from their respective substitutional Ga sites and coalesce together forming MnAs islands.

In this study a unique multistep etching/deposition process utilizing porous alumina as a direct deposition mask was developed and used to make confined disks of GaMnAs on a GaAs substrate. This marked the first time that GaMnAs was studied in its confined state, and demonstrated a technique that can be used to create confined nanostructures of *any* thin film without being restricted by modes of self-assembly.

EXPERIMENTAL:

The multistep process starts with the growth of a GaMnAs thin film on a desorbed GaAs substrate. To pattern the film into confined nanodisks a separately synthesized porous alumina mask is floated onto the surface and Cr is deposited throughout the pores onto the surface. The alumina is etched away leaving behind an array of Cr dots on the surface that acts as an etch mask for argon plasma etching. The end result is an array of Cr dots on top of disks of GaMnAs.

Molecular beam epitaxy (MBE) was used to create a high crystalline quality thin film of GaMnAs. The following steps were performed in-situ in an MBE chamber. First a semi-insulating GaAs (001) substrate was desorbed of its native oxide by heating it to ~ 700 °C under an As flux. Then, a 10 nm thick buffer layer of GaAs was deposited at 580 °C to make a well-ordered high crystalline quality backing for the GaMnAs film. Then, a 15 nm thick $Ga_{1-x}Mn_xAs$, $x = 0.07$, layer was deposited at a substrate temperature of 255 °C. This low temperature was crucial for maintaining a homogenous distribution of Mn throughout the system. If not for this low temperature, the Mn could migrate to the surface and coalesce forming MnAs islands. After GaMnAs was deposited on the surface, the sample was removed from the chamber and annealed in air for 20 min at 230 °C. This last step was performed to increase the films ferromagnetic Curie temperature by decreasing the Mn interstitials.^{24,25}

Before any further processing was done to the sample, magnetic and thermomagnetic characterization was done via a SQUID magnetometer (Superconducting Quantum Interference Device). The magnetic moment of the film was measured in-plane as a function of temperature in the range of $T = 10 - 200$ K. Figure 1 shows the temperature dependence of the magnetization decaying up to a Curie temperature of $T_c = 140$ K. This ferromagnetic transition temperature is typical for low-temperature annealed GaMnAs. The inset of Figure 1 shows the magnetic hysteresis at $T = 70$ K with a coercive field of $H_c = 6$ Oe. These values will later be compared to the temperature dependent magnetization after further processing into nanodots. The most importance point to take from these values is that the film was ferromagnetic before any further processing was done to it.

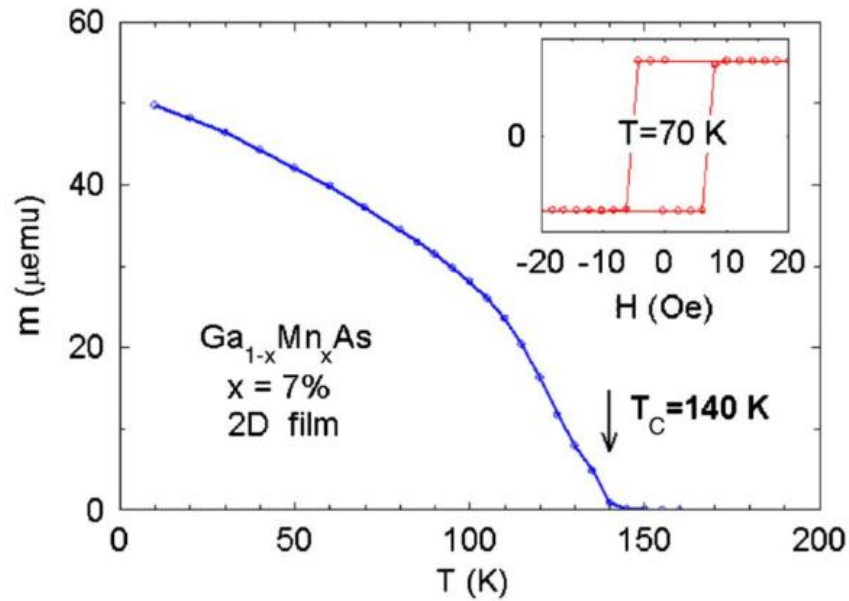


Figure 1: Magnetic moment vs temperature for a ferromagnetic 2D film of $\text{Ga}_{1-x}\text{Mn}_x\text{As}$ and $x=0.07$ in an applied magnetic field of 5 Oe. The moment drops to zero at the ferromagnetic Curie temperature, $T_C=140$ K. The inset shows the ferromagnetic hysteresis at $T=70$ K.

The next step was to make the porous alumina mask that will be used to mask the deposition of Cr onto the surface of the GaMnAs epitaxial film. To make the porous alumina mask a high-purity Al foil is anodized at a constant voltage of 40 V in a 3% oxalic acid and water solution. This first anodization was carried out for 10-12 hours, creating an alumina surface on the foil that is structured with highly-ordered pores. Since the bottom of these pores has the best ordering, the alumina is etched away using a chromic-phosphoric acid to leave a dimple pattern on the Al surface that is highly ordered. Next, the surface that is decorated with an array of dimples is reanodized for a short time in the 3% oxalic acid creating a second alumina layer with high aspect ratio pores. The next step is to remove the aluminum which is now the backing for the pores. This is done by first coating the porous side of the Al with an organic varnish layer (GE-7031 varnish). This protects the pores from being etched away when it is dipped in a saturated HgCl_2 solution to remove all the aluminum from the structure. Then a 5 wt.% phosphoric acid dip for 80 min is used to open up the ends of the pores. Lastly, IPA (isopropyl alcohol) is then used to remove the varnish from the surface. Using a SEM (Scanning Electron Microscope), the pore sizes and measurement of the thickness can be obtained. Figure 2(a,b) shows micrographs of the porous alumina mask from both a top-down perspective (a), and a cross section (b). Using these micrographs we obtain estimates of the pore diameter (~ 40 nm),

pore spacing (~ 80 nm) and mask thickness (~ 400 - 800 nm). At this point the porous alumina masks are ready to be placed on the surface of the GaMnAs film.

Though barely visible to the naked eye, the porous alumina masks can be floated in an IPA solution and dried on the surface of the GaMnAs epitaxial film. Figure 2(b) shows a cross-sectional SEM micrograph of a position on the GaMnAs surface where the mask has lifted slightly away from the sample. A piece of lens tissue can be used to transport and store the masks. Transport and transfer of the masks proves to be a difficult task because the alumina is extremely thin and brittle. Improvement of this process in the future, though, could lead to a gentler and mass producible manufacturing process.

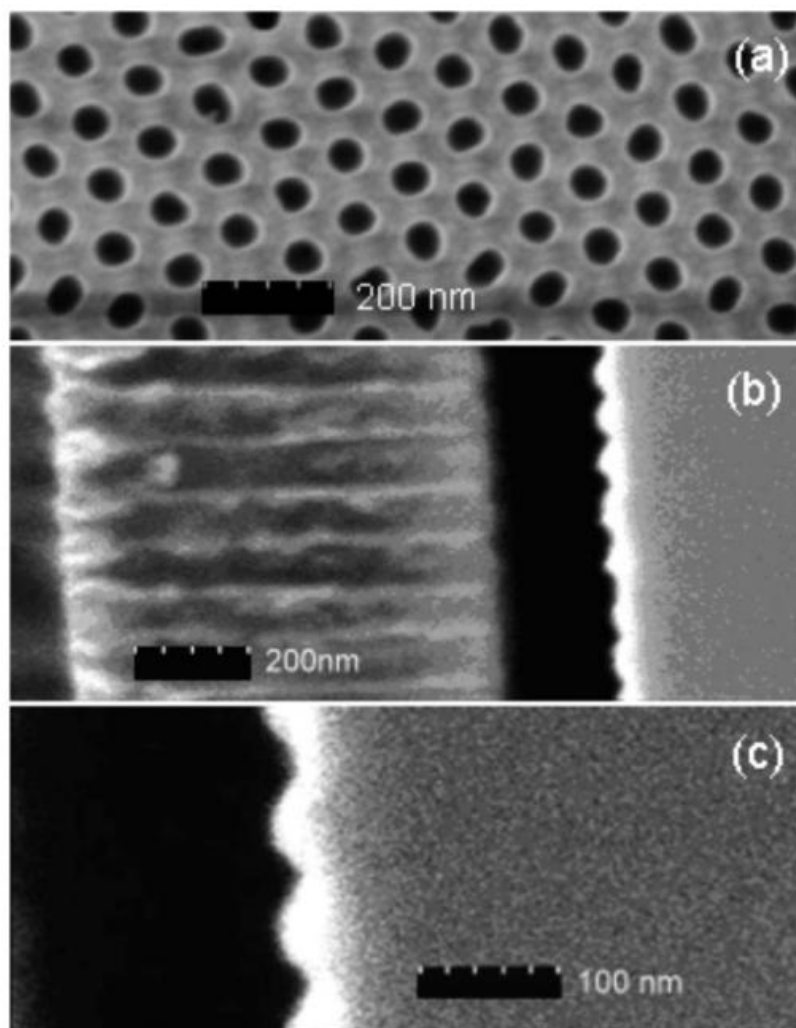


Figure 2: SEM micrographs. Those shown are: (a) anodic porous alumina mask, (b) cross section of the porous alumina mask lifted away from the substrate (left) and the Cr nanodots that were deposited on the substrate through the pores (right), and (c) side view of the GaMnAs/Cr nanodots after plasma etching.

After the mask is floated onto the surface and dried, the sample is mounted in a vacuum chamber for thermal evaporation of chromium through the pores. Cr was chosen because it's paramagnetic and has a much lower etch rate than the surrounding GaMnAs film. The paramagnetism of the Cr can be subtracted from the overall moment of the sample when measuring the characteristics of the nanodisks. The Cr was deposited in a vacuum of 7×10^{-7} torr via thermal evaporation at a rate of ~ 0.1 nm/sec until a total thickness of 40-45 nm was produced. The growth rate and thickness were determined using an in-situ crystal monitor. Despite the relatively high aspect ratios of the pores in the porous alumina, with length/diameter of ~ 10 -20, the Cr had enough mobility at room temperature to migrate all the way down the pores and deposit on the substrate beneath. By looking at the SEM image in Figure 2(b) one can see that the top sides of the pores in the mask are covered with a brighter material. This is a buildup of Cr which eventually impeded the flow through to the bottom of the pores. This impedance accounts for the smaller height of the dots (~ 35 nm) compared to the as-deposited thickness of the Cr layer (40-45 nm). After deposition, the mask was dissolved away in a 5% phosphoric acid solution for about 5 minutes leaving behind the now exposed array of Cr nanodots on the surface (Figure 2(c)). Lastly, plasma etching was used to etch away the unwanted GaMnAs film around the Cr nanodots. For this a South Bay Technology RIE 2000 reactive ion etcher was used. Since the etch rate of the Cr is much higher than that for GaMnAs the etching duration was just long enough to sufficiently remove the underlying 15 nm of GaMnAs film. The appropriate etching times were several hours in an argon plasma with a pressure of 100 mtorr.

RESULTS:

The main goal of this study was to explore the magnetic characteristics of GaMnAs when under confined geometries. To do this the sample was placed in a SQUID magnetometer and, like with the thin film magnetic characterization, the magnetization was obtained as a function of temperature. The sample was mounted in such a way as to orient the substrate plane and dot diameters parallel to the applied field (H).

In order to fully characterize the magnetic state of the nanostructures it is necessary to compare the temperature-dependent magnetic moment $m(T)$ for the ZFC and FC conditions. In both cases the sample was cooled to $T = 5$ K, but in the FC condition a field of $H = 100$ Oe was applied for the

duration of the temperature sweeps. A comparison between these two plots gives a solid understanding of how the sample's magnetic moment is affected by temperature. The ZFC measurement was taken by first cooling to $T = 5$ K in zero applied field, then a field of $H = 100$ Oe was applied and the temperature was raised back to room temperature. The data in Figure 3 shows both the ZFC and FC curves as being linear above a Curie temperature of $T_c \sim 90$ K. However, below $T = 60$ K there is a clear difference in magnetization between the FC and ZFC graphs. The decrease of the ZFC moment at low temperatures shows that the material has lost its spontaneous ferromagnetic ordering. This deviation is a signature of superparamagnetism.^{26,27} Superparamagnetism is a consequence of the small magnetic moment of nanometer sized ferromagnetic particles and a signature of reduced dimensions. The maximum of the ZFC is identified at a blocking temperature of $T_b = 30$ K. What this blocking temperature does is set a temperature threshold that separates the ferromagnetic behavior from paramagnetic behavior. Below this temperature the nanodots are ferromagnetic. Their hysteresis at $T = 4$ K can be seen in the inset of Figure 3. At $T = 4$ K the magnetization hysteresis saturates at $H_s \sim 1000$ Oe and has a coercive field of $H_c = 130$ Oe.

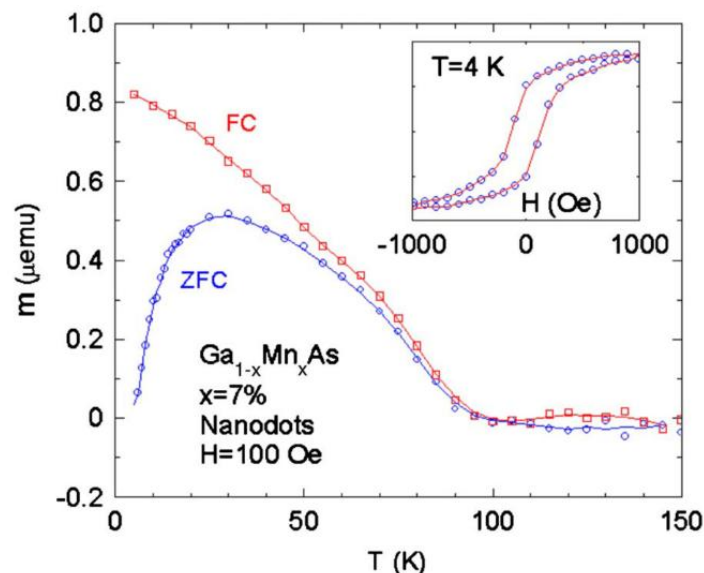


Figure 3: Magnetic moment vs temperature of a GaMnAs nanodot array in an applied field of $H=100$ Oe. The FC and ZFC data are shown, revealing superparamagnetic behavior with a blocking temperature of $T_B=30$ K. The inset shows the ferromagnetic hysteresis at $T=4$ K.

Measurements were made with the applied field both in-plane and out of plane. A hard axis for the nanodots was found to be out of plane. This confirms that the dots have the same anisotropy as that of 2D films²⁸. This is due to the in-plane shape anisotropy.

It is important to note though that for fields applied in the plane of the disk-like nanodots no

discernable difference was found between the [110] and [1₋10] crystalline directions. This is unlike the GaMnAs 2D film, and can be explained by the uniaxial anisotropy in 2D films (which depends on temperature, Mn concentration and annealing conditions).²⁹ The reduced in-plane anisotropy in the confined dots is due to changes in the relative magnitudes of the biaxial (K_c) and the uniaxial (K_u) anisotropy constants. For the nanodots it appears that the uniaxial anisotropy may be much smaller than the cubic anisotropy in the temperature region of interest. An effective anisotropy constant for the nanodots can be deduced from the blocking temperature, where the ratio of anisotropy energy to the thermal energy is given by,

$$\frac{K_1 V}{k_B T_B} = 25 \quad \text{with} \quad V = \pi D^2 \frac{H}{4}$$

For the dot diameter $D=40$ nm, height $H=15$ nm, and $T_b=30$ K, $K_1 \sim 6000$ ergs/cm³. This is of the order of the magnitude found for the 2D epitaxial layer.

CONCLUSIONS:

The development of this fabrication procedure has allowed for the study of GaMnAs in its confined dimensions. The required low temperature growth hinders the ability for GaMnAs to form into nanostructures via self-assembly without altering its inherent crystal structure, atomic arrangement, homogeneity and atomic concentrations. Without the use of porous alumina, the Cr etch mask could not have been patterned on top of the GaMnAs film under the proper size constraints.

This was the first time that GaMnAs was fabricated under these confined geometries and their magnetic characteristics studied. The GaMnAs disk-like nanodots showed the characteristics of superparamagnetism. There was a blocking temperature where the ZFC moment was low and a ferromagnetic hysteresis was evident at low temperatures ($T = 4$ K).

Not only does this mark the first time that GaMnAs was studied under confined dimensions, but it outlines a process for fabricating other alloy thin films in a confined geometry without having to alter the growth conditions. Also, unlike self-assembly, this technique creates highly-organized arrays of nanostructures. Long-range order is vital in device manufacture for spintronics applications. Advances in the use of porous alumina as etch template may also lead to a commercial process that can mass produce nanostructures of this size without the use of complicated and time consuming lithography techniques.

II. Universal properties of linear magnetoresistance in strongly disordered MnAs-GaAs composite semiconductors²

All materials have structural crystalline defects. According to thermodynamics it is statistically improbable that macroscopic materials can be created with a defect concentration of zero. However, we can utilize these defects in a practical way that forms the backbone of many advanced technological applications. A simple example is that of the hardening of steel. To make a steel alloy stronger one introduces defects into the crystal lattice. Even in medieval times this technique was used to introduce dislocations into the crystal lattice and it was known as work hardening. When a blacksmith pounds a red hot steel bar with a sledge hammer he is not merely trying to change the shape of the material, but rather introduce dislocation defects into the crystal structure of the alloy. This in turn results in mechanically hardening the material, making it a stronger weapon.

But there are many other characteristics, other than mechanical strength, that change when introducing imperfections into a material. By introducing disorder into a thin film magnetic, electronic, magnetoelectronic and thermomagnetic characteristics can be changed drastically. Harnessing these effects to work to our advantage is vital to understanding 2D electronic systems. Understanding these effects can also help to eliminate current hurdles imposed by high temperature materials operation. Much study has been done on transport properties of materials at low temperature showing a lot of promising characteristics for device technologies. But these effects often disappear at room temperature due to the effects of phonon scattering. If we can understand these effects of electron transport at room temperature these problems might be worked around to enable the use of low temperature effects at 300 K. This study outlines a leap in the right direction in the overall drive to understand electron transport in disordered systems and hopefully, in the end, recognize a universal electron transport theory for macroscopically disordered systems of all types.

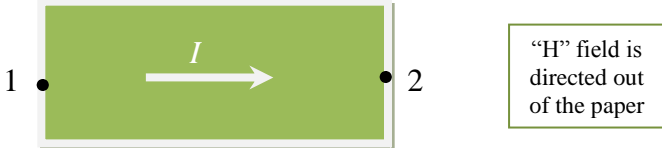
In this study it was observed that the linear magnetoresistance (LMR) that occurs in semiconductors is a consequence of strong electrical disorder. By investigating a disordered MnAs-GaAs composite thin film, it was found that *the magnitude of the LMR is numerically equal to the carrier mobility* over a wide range, and is independent of carrier density. This behavior is complementary to the Hall Effect, (which is independent of the mobility and directly dependent on the carrier density). Moreover, the LMR appears to be insensitive to the details of the disorder and points to a universal explanation of classical LMR that can be applied to other material systems.

BACKGROUND:

Materials and systems that show a predictable magnetoresistance are vital for the production of new nonvolatile magnetic storage devices and small scale magnetic field sensors. It is already well known that thin film homogenous semiconductors display a relatively classical response when measuring magnetoresistance. Typically they will show a quadratically increasing resistance response to an increasing magnetic field. This response will also saturate at high field holding a constant resistance up to the highest fields. On the other hand it has been recently found that in compositionally inhomogeneous semiconductors having strong electrical disorder, the magnetoresistance will be anomalously large; increasing linearly with increasing field without showing any signs of saturating at high fields.^{30,31,32,33} Like with the AgSe system which exhibited a remarkably high LMR, up to $H = 55\text{T}$, the cause of the LMR behavior was the electrical disorder of the system. In AgSe the cause was the presence of insulating or metallic nanoparticles in the matrix hindering the overall electron mobility of the system.

This linearity has been seen already in thin film systems and its explanation was attributed simply to the electrical disorder of the system. Through studying the transport properties of the GaAs-MnAs composite semiconductor system in detail there appears a clear direct correlation between the LMR and the fundamental electrical properties of the system.

First off, it is important to understand magnetoresistance and how it is measured. It is defined as being a function of the applied magnetic field and determined via the field dependent transverse (current perpendicular to magnetic field) resistance as $R(H)$ as;

$$MR_H = \frac{R_H^{1-2} - R_{H=0}^{1-2}}{R_{H=0}^{1-2}}$$


The diagram shows a green rectangular sample with two terminals, labeled 1 and 2, on its left and right sides respectively. A white arrow labeled 'I' points from terminal 1 to terminal 2, representing the current flow. To the right of the sample, a text box with a green border contains the text: "H" field is directed out of the paper.

The magnitude of the LMR is found to be numerically equal to the magnitude of the macroscopic carrier mobility over a wide range of temperature and mobility. This equality,

$$MR_T = \mu_T H ,$$

is obeyed despite changes in temperature which alter the carrier concentration by several orders of magnitude. This shows that LMR is governed by carrier mobility at a constant temperature (due to the

macroscopic disorder). It also, in this effect, serves as a compliment to the Hall effect that is governed dominantly by carrier concentration (see Figure 4).

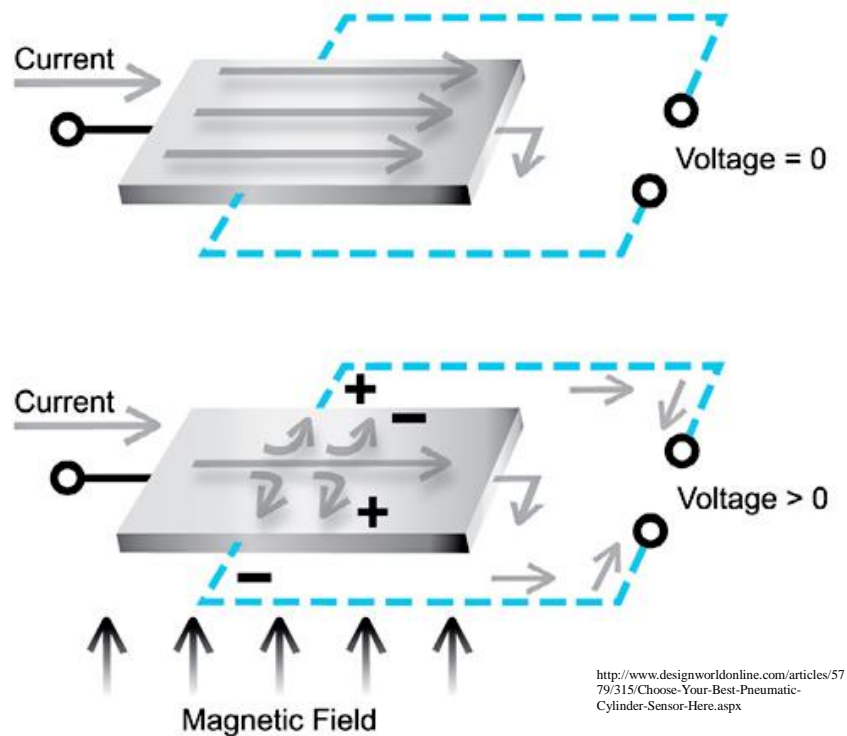


Figure 4: Diagram showing how the Hall effect is measured via a pictorial representation of charge motion across a thin film sample.

This dependence on carrier concentration becomes more apparent by the figure. Unlike the magnetoresistance, the Hall voltage is dependent on the overall concentration of the offset carriers manipulated by the field.

Additionally it was found that the actual nature of the disorder in the system doesn't affect the relationship between mobility and LMR. This was found by comparing results from multiple samples with varying size and concentrations of disordered regions. This points directly to a universal description of MR in semiconductors with high degrees of disorder.

EXPERIMENTAL:

The magnetoresistance measurements were conducted on composite thin films of GaAs embedded with MnAs nanoparticles. The samples were fabricated starting from thin layers of molecular beam epitaxy (MBE) grown $Ga_{1-x}Mn_xAs$, $x=0.1$. They were grown at a low temperature (250

°C) in order to limit the Mn mobility during growth. This allowed us to create a high quality crystalline lattice. Then a subsequent in-situ anneal was performed that enabled the formation of MnAs nanoparticles in the GaAs matrix via self-assembly.^{34,35} The annealing temperatures used were 500-700 °C for 30 min in the MBE chamber with an arsenic flux at a vapor pressure of 10^{-6} torr. Many samples were prepared but those that were annealed in temperatures ranging from 570-670 °C showed the most robust LMR characteristics. These samples were characterized by scanning electron microscopy (SEM), superconducting quantum interference magnetometry (SQUID), atomic force microscopy (AFM), and x-ray diffraction (XRD). The transverse MR was measured with the magnetic field perpendicular to the current direction. Note that this is also the orientation that puts the field perpendicular to the sample surface as well.

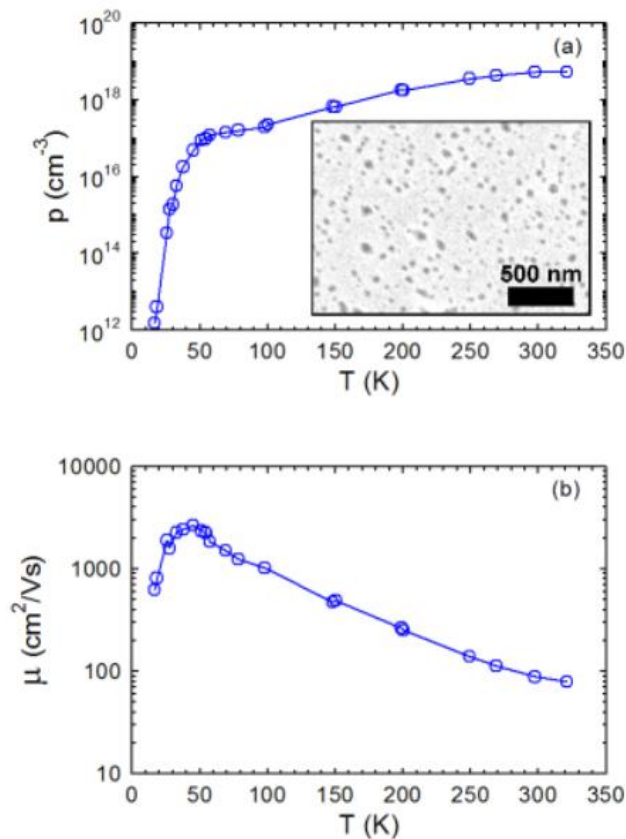


Figure 5: Temperature-dependent electrical transport properties of MnAs-GaAs self-assembled composite films. [(a) inset] SEM micrograph of a self-assembled composite film depicting MnAs nanoparticles of diameter 20-80 nm (50 nm average diameter) dispersed in the GaAs matrix, where the bar is 500 nm. (a) Plot of the density of mobile holes versus temperature, $p(T)$, obtained from Hall-effect measurements, highlighting carrier freeze out at low temperature. (b) Plot of hole Hall mobility versus temperature, $\mu_h(T)$, showing a slowly increasing carrier mobility with decreasing temperature, from the room-temperature value of $\mu_h=100 \text{ cm}^2/\text{V}\cdot\text{s}$ (obtained from Hall effect measurements).

The inset of Figure 5(a) shows a SEM micrograph of one of the samples. The dark spots in the image are the MnAs nanoparticles. Their diameters range from 20-80 nm with an average particle size of 50 nm, (for size distribution studies see sec. #3). These sizes could put the MnAs nanoparticles' magnetic characteristics in two different categories; superparamagnetic at smaller diameters and ferromagnetic for larger. We find, though, that the magnetic nature of the nanoparticles does not affect the magnetoresistance for temperatures greater than $T=50$ K. In actuality, it turns out that the difference between the conductivity of the nanoparticles and the surrounding crystalline matrix is responsible for the linear-in-H magnetoresistive response.

The electrical transport properties of one of the samples (a 20 nm composite film) are also shown in Figure 5. These show that conduction in the film is dominated by the high density of holes introduced by the Mn atoms in the matrix. Figure 5(a) plots the hole density as a function of temperature that was determined via Hall effect measurements. The Hall effect sends the positive holes to one side due to Lorentz force interactions (via the right-hand rule), (see Figure 4). Near room temperature the hole density is thermally activated from Mn acceptor sites whose density has been measured to be $p_a = 4 \times 10^{19} \text{ cm}^{-3}$, with an activation energy of $E_a = 108 \text{ meV}$ by D. Heiman.³⁶ As the temperature decreases, the holes become trapped on the acceptors. Figure 5(b) plots the mobility as a function of temperature $\mu_H(T)$. Near room temperature the mobility is $\mu_H = 100 \text{ cm}^2 / \text{Vs}$ and increases with decreasing temperature due to reduced phonon scattering, but below $T \sim 50$ K it decreases sharply. This sharp decrease coincides with a rapid freeze out of carriers.

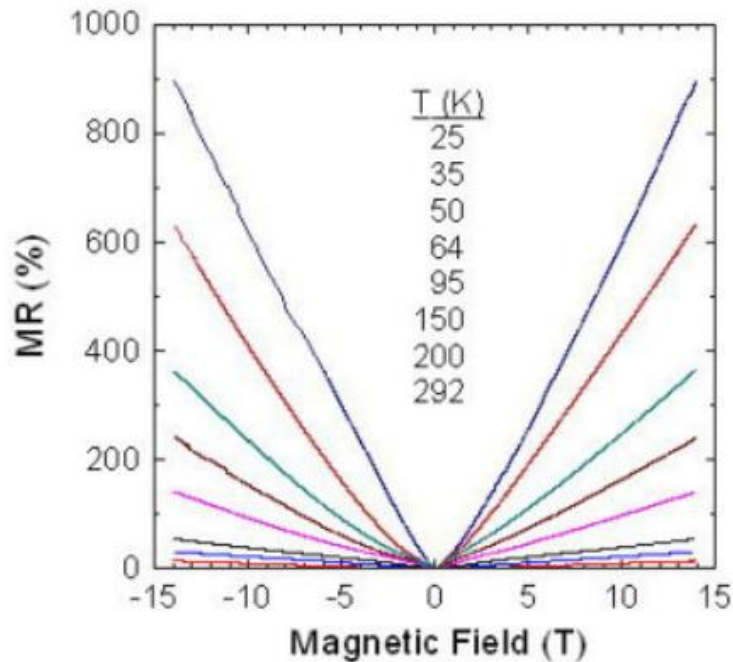
RESULTS:

Figure 6: Transverse magnetoresistance of MnAs-GaAs self-assembled composite film versus applied magnetic field (H) at various temperatures (T). The magnetic field is applied perpendicular to the plane of the film in which the current was flowing. For increasing field, the variation in the MR is proportional to the H^2 and quickly becomes linear in field at higher fields. For increasing temperature the MR increases from a value of $MR=14\%$ at room temperature to 900% at $T=25$ K.

Figure 6 shows the experimentally obtained MR as a function of field at different temperatures of one of the composite film samples. The low field dependence of the MR follows a quadratic dependence, but at higher fields becomes linear. This linear response at high fields is found to be present at all temperatures measured, $20\text{ K} < T < 300\text{ K}$, and at the highest field of 14 T the response skyrockets from 14% at room temperature to nearly 1000% at $T=25$ K. This is visualized by plotting the slope of the linear portion of the response as a function of temperature (from 5 T to 14 T). In Figure 6 the slope, — is plotted as a function of the inverse of temperature (—) as the solid blue circles. A straight line through the data is a fit to the data as it follows a power law dependence given by — . On top of this is plotted the hole mobility found earlier in Figure 5(b), but plotted as a function of — . It is the close relationship between these two plots that made us realize the seminal connection between the carrier mobility and linear magnetoresistance (see Figure 7).

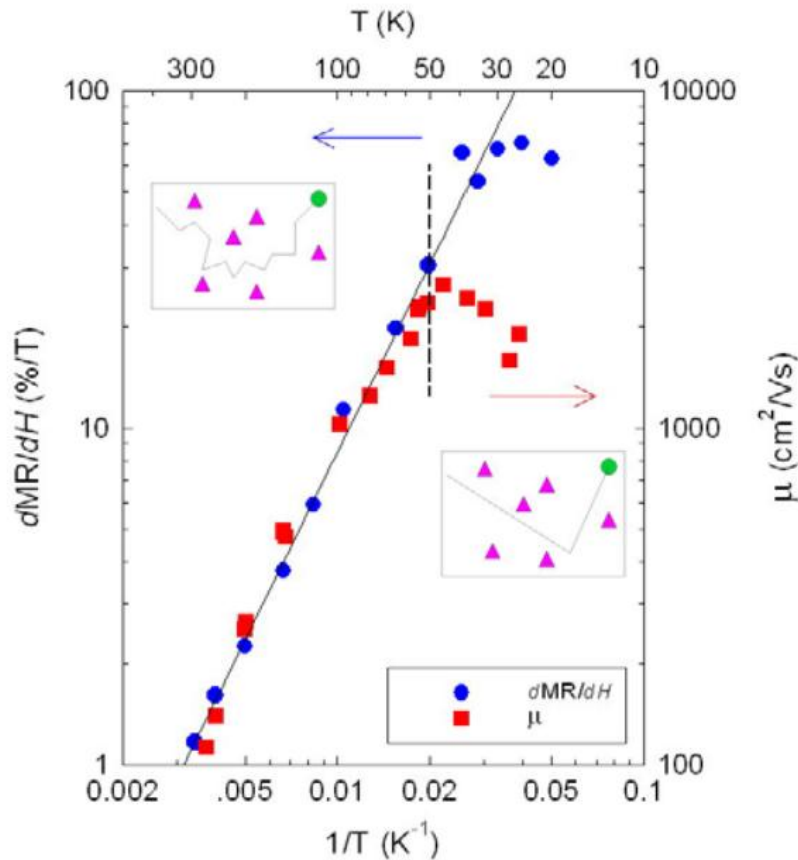


Figure 7: Linear magnetoresistance and hole mobility of MnAs-GaAs self-assembled composite film plotted as a function of inverse temperature, $1/T$. The magnitude of the linear magnetoresistance, expressed as the derivative of the MR at high fields, dMR/dH , is shown by the blue solid circles. The hole mobility, $\mu_h(T)$, obtained from Hall-effect measurements, is shown by the red solid squares and has been scaled to overlay the magnetoresistance values. Both of the quantities have identical temperature dependencies, $dMR/dH(T) = \mu_h(T)$ and the solid line through the data is a power law. The dashed line marks the temperature where the carrier mean-free path is equal to the average nanoparticle spacing, illustrated in the insets. *Dashed line shows temperature where the LMR deviates from the carrier mobility. Image insets show how above this temperature (blue arrow) the MR is dominated by phonon scattering, but below it (red arrow) the carriers mean free path is too long due to phonon scattering for the disorder to have an effect.

It is remarkable that the hole mobility and the slope of the magnetoresistance for this range of temperatures have identical power law relationships. Not only that, but they both exhibit the same saturation behavior at low temperatures; where both have a common maximum near $T \sim 40$ K. Below $T = 50$ K the mobility is no longer dominated by phonon scattering and the turnover of the LMR slope data coincides with the rapid carrier freeze out. From Figure 7 it is clear that the identical temperature dependencies of the LMR and the mobility unambiguously demonstrate that the MR is linearly

proportional to the carrier mobility. Furthermore, by adjusting the scales to overlap the two sets of data it is seen that the two parameters are numerically equal, $MR(T) = \mu(T)H$; a remarkably universal result. It is also noted that this relation holds as temperature is changing and therefore remains unaffected by changes in carrier density of several orders of magnitude. This means that LMR is *independent* of carrier density, unlike the Hall effect which is proportional to the carrier density).

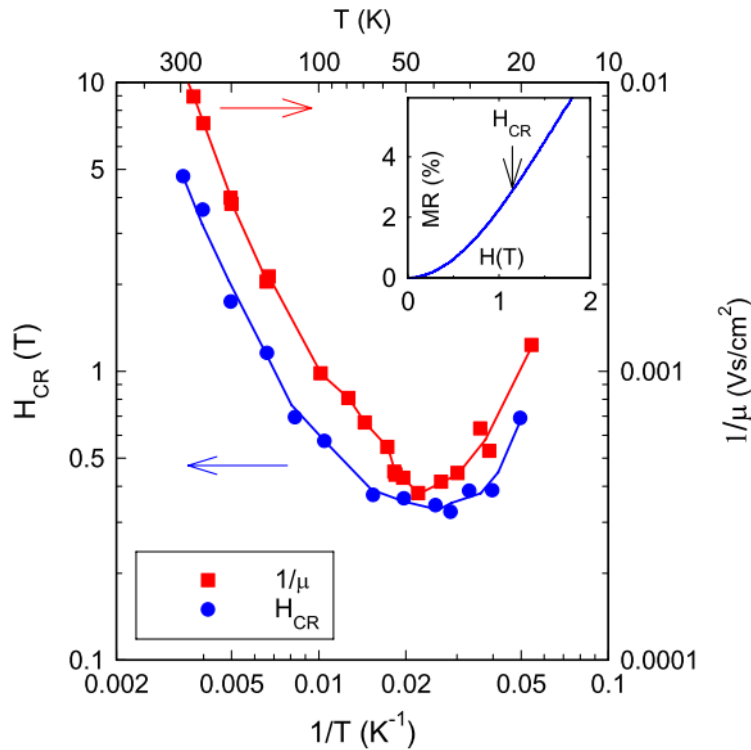


Figure 8: Crossover field, H_{CR} , and inverse hole mobility, $1/\mu_h$, of a MnAs-GaAs self-assembled composite film versus inverse temperature, $1/T$. H_{CR} is defined where the magnetoresistance crosses over from a quadratic H^2 dependence at low fields to a linear-in- H dependence at high fields, shown in the inset for $T=150 \text{ K}$. $H_{CR}(T)$ is shown by the blue solid circles. The inverse hole mobility obtained from Hall effect measurements is shown by the red solid squares and has been scaled to lie close to the crossover field values. The quantities have closely matched temperature dependencies, $H_{CR}(T) \propto 1/\mu_h(T)$.

Even more evidence that links MR to carrier mobility is the crossover field, $H_{CR}(T)$, where the makes a transition from quadratic to linear dependence in H . This transition was determined by fitting the MR data to a second order polynomial in H . The inset of Figure 8 shows the position determined for the $H_{CR}(T)$, where $T=115 \text{ K}$ and $H_{CR}=1.15 \text{ T}$. This crossover field is then plotted as a function of temperature and compared to the inverse of hole mobility³⁷ (previously found by Hall effect measurements). Figure 8 shows this plot and clearly demonstrates a close connection between H_{CR} and

μ , including a direct correlation between their respective minima; both at 40 K. This correlation shows that for all temperatures the crossover field is linearly proportional to the inverse of hole mobility, $MR(T) \propto 1/\mu(T)$. This is yet another result that points to carrier mobility as being the inherent material characteristic responsible for all magnetoresistance behavior.

DISCUSSION:

All the experimental data for these MnAs-GaAs composite systems points to how the magnetoresistance and crossover field as functions of temperature are governed by the macroscopic carrier mobility of the system. These experimental realizations reflect the theory generated by Parish and Littlewood in 2005.³⁸ Their predictions centered on building an FEA (finite element) model of an inhomogeneous conducting media.

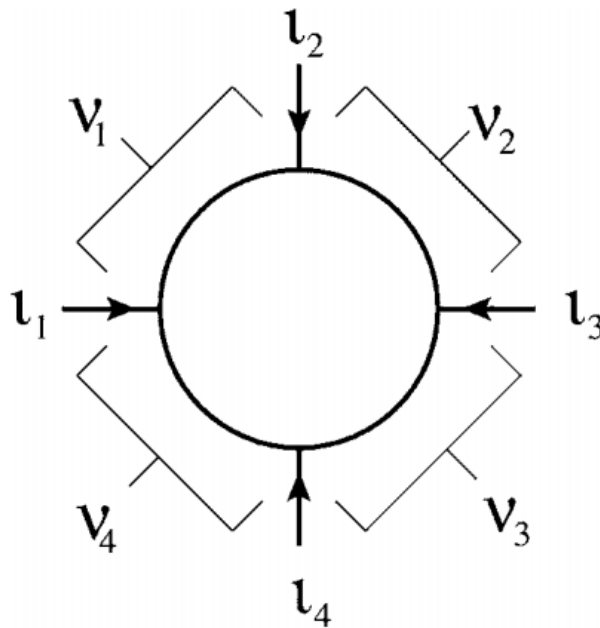


Figure 9: Diagram of the finite unit used to model a resistor network. "The network consists of a homogenous, conducting disk with four equally spaced terminals. Currents entering the disk are taken to be positive, while the voltage differences, v , between the terminals are considered positive when measured in the clockwise direction." From Parish and Littlewood (2005)³⁸

The discretized components for this model were made up of couple 4-terminal elements. The elements were taken to be simple resistors based on a circular disk, (van der Pauw resistors) (see Figure 9). The actual element geometry that they used didn't necessarily need to be a disk but this 3D shape was used for simplicity. For an infinite network of these elements there was found to be a linear-in-H resistive response. The model also predicts that the MR is dominated either by the average mobility, $\langle\mu\rangle$, **OR** the width of the mobility distribution, $(\Delta\mu)$. When $\frac{\Delta\mu}{\langle\mu\rangle} > 1$ (both the MR and H_{CR} are expected to be a function of the width of the mobility variation, $(\Delta\mu)$. The width of the mobility variation can be explained as being the actual variation of the disorder. If the disorder is uniform, aka there are equal regions of both electrons and holes, the average mobility vanishes ($\langle\mu\rangle = 0$). This behavior is attributed to the AgSe system by J. Hu *et. Al.* (2007)³⁹, where their AgSe particle distribution showed an equal proportion between regions of electrons and regions of holes. On the other hand, the AgSe system made by M. von Kreutzbruck *et. Al.* (2009)⁴⁰ had a narrow mobility width. The percolating conductivity between their silver grains was responsible for their $\frac{\Delta\mu}{\langle\mu\rangle} < 1$. By this rationale the dependence that our MnAs-GaAs composite system displays points at a narrow mobility distribution $\frac{\Delta\mu}{\langle\mu\rangle} < 1$.

The mean free path of the charge carriers and the length scale of the disorder are two statistics that work hand in hand to result in the linear dependency phenomena. At higher temperatures, $T > 50$ K, the mean free path length is dominated by phonon scattering, ($L_{mfp} \cong 10 - 100$ nm). But once the temperature decreases below $T = 50$ K the mean free path lengthens and, coincidentally, the LMR deviates from the mobility (refer back to image insets in Figure 7). This would make sense since the L_{mfp} would become larger than the average MnAs particle separation of $\langle d \rangle \approx 100$ nm (see diagram insets of Figure 7). When this occurs and $L_{mfp} > \langle d \rangle$ the classical model by Parish and Littlewood also breaks down. Other than the temperature affecting the point where the mobility and LMR deviate, we found that the nature of the disorder (particle size and average particle separation) did not change the universal relationship between the two. In the regime where the mean free path was small (above $T = 50$ K), the magnitude of the LMR was identical for several samples with varying particle sizes and

densities. This means that the dimensional details of the disorder are not important for the production of a LMR response. Rather it is the relation $L_{mfp} > \langle d \rangle$ being met that is important for generating LMR, (d = length scale of inhomogeneities).

CONCLUSIONS:

The results presented here on the magnetotransport properties of composite MnAs-GaAs films show that the linear magnetoresistance is governed strictly by the average macroscopic carrier mobility. The realization of this also uncovered the complementary relationship present between the Hall effect and LMR; whereas, the Hall effect is proportional to the carrier density and independent of mobility (concluded from temperature studies). These observations show convincing support for a universal model connecting the magnetotransport and thermomagnetic properties of strongly electrically disordered semiconductors.

III. Determining magnetic nanoparticle size distributions from thermomagnetic measurements³

As research continues to explore the characteristics of magnetic nanoparticles and their synthesis, new methods of investigation have to be developed. Once a ferromagnetic material is confined to nanometer dimensions (as realized in section I.) its magnetic properties can change drastically. In order to understand the properties of these nanometer size ferromagnets one must categorize the size distribution of nanostructures found in the ensemble. Current means to extract a size distribution from a sample of magnetic nanostructures rely on extensive scanning electron microscope studies. SEM or TEM (Transmission Electron microscopy) micrographs are taken throughout the sample and the sizes of the particles are measured. Scouring images of nanoparticles takes considerable time and introduces a human error into the measurement. This measurement method is also restricted to what one can see on the surface. For samples with embedded nanostructures there is currently no way to obtain a size distribution without destroying/removing parts of the sample.

In this study thermomagnetic measurements are used to obtain the size distribution and anisotropy of magnetic nanoparticles. An analytical transformation method is described that utilizes temperature dependent ZFC (zero-field cooling) magnetization data to provide a quantitative measurement of the average diameter and relative abundance of superparamagnetic nanoparticles.

We then apply this method to a system of MnAs nanoparticles in a GaAs matrix, which reveals a log-normal size distribution and reduced anisotropy for nanoparticles compared to bulk materials. In doing so we attain the uniaxial magnetic anisotropy constant for MnAs and find that it is substantially smaller for nanoparticles than for the bulk system. This analytical technique holds promise for rapid assessment of the size distribution of an ensemble of superparamagnetic nanoparticles.

BACKGROUND:

It is already known that the average particle size in an ensemble of magnetic nanoparticles can be estimated from magnetic measurements by several methods, such as fitting the field-dependent magnetization, $m(H)$, to a classical Langevin function.⁴¹ In some systems the average particle size of superparamagnetic nanoparticles can be estimated from the thermal blocking temperature, T_b . While these measurement techniques identify the average diameter of an ensemble of magnetic nanoparticles they do not quantify the overall distribution of the nanoparticle diameters of the system.

METHODS:

In this study we demonstrate a technique for approximating the size distribution of superparamagnetic nanoparticles in a system via the data obtained from thermomagnetic measurements. This transformation method makes use of an approximation to convert the measured temperature-dependent ZFC magnetic moment, $m_{ZFC}(T)$, into a probability distribution of particle size. The method was tested on a system of MnAs nanoparticles in a GaAs matrix, (a system identical to that used in sec. #2). To verify the approximation method the particle distributions were determined analytically by a series of SEM micrographs taken across the sample surface.

Our method is based on the Néel model⁴², which describes the relaxation of non-interacting, single-domain magnetic nanoparticles that experience uniaxial anisotropy. Uniaxial anisotropy results in a double-well potential for the two directions of moment alignment. The two wells are separated by an energy barrier E_B , which (in the superparamagnetic state) can be overcome by thermal activation with a relaxation time τ ,

$$\tau = \tau_o \left(\frac{E_B}{K_B T} \right),$$

where $1/\tau_o$ is the attempt frequency. In the small field limit $E_B = K_{eff} V$, where K_{eff} is the effective anisotropy constant and V is the particle volume. The most commonly used equipment, and that which we use, is a SQUID magnetometer. It's $\tau \approx 10^2 s$ and the attempt time is $\tau_o \approx 10^{-9} s$, so the ratio of the anisotropy energy to thermal energy is therefore commonly given by,

$$K_{eff}V/k_B T_B = 25 \quad (1)$$

Within the assumptions of the model, this equation allows for the assumption of the magnetic volume V of a particle when K_{eff} is known, (and vice versa).

There are, however, a few limitations of this method that must be pointed out. The magnetic field applied to the sample during the ZFC sweep must be small compared to the samples anisotropy field so that it does not lower the effective barrier height, (in most instruments this field is as low as earth's magnetic field). Also it neglects particle to particle magnetic interaction. If the particles are close enough their interaction would raise the apparent blocking temperature⁴³. Lastly, complications arise when multiaxial (cubic) anisotropy is evident in the nanoparticles, which may result in a reduced effective barrier height.

Computation of the functional distribution of the particle volume $f(V)$ or particle diameter $f(D)$ can be extracted from the $m_{ZFC}(T)$ data curve. This is because each individual nanoparticle in the system is characterized by a unique blocking temperature, T_B , through equation (1). The overall moment of the nanoparticles in the system is given by,

$$m_{ZFC}(T) = \frac{Hm_s^2(T)}{3k_B T} \int_0^T f(T_B) dT_B, \quad (2)$$

where m_s is the total saturation moment and its temperature dependence can be neglected for materials with Curie temperature $T_c \gg T_B$. Solving equation (2) for $f(T_B)$ yields the approximation,

$$f(T_B) \propto \frac{1}{V^2} \times \frac{d}{dT} [Tm_{ZFC}(T)]. \quad (3)$$

Finally, assuming spherical particles, the distribution in particle diameter, $f(D) \propto f(T_B) \left(\frac{dT_B}{dD} \right)$, is

computed using equation (1) with $V = \frac{\pi D^3}{6}$.

To test the accuracy of the approximation method, equation (3) was evaluated assuming a log-

normal distribution, $f(D) \propto \left(\frac{1}{D\sigma}\right) \times e^{\left(\frac{-[\ln(D)-\mu]^2}{2\sigma^2}\right)}$, using a range of standard deviations (relative distribution width). These $f(D)$ were then used to plot the $m_{ZFC}(T)$ with equation (2), followed by computing $f(D)$ again via equation (3). This turned out to reproduce the log-normal distribution from the method. However the mean particle diameter, $\langle D \rangle = e^{\left(\mu + \frac{\sigma^2}{2}\right)}$, and the distribution width were slightly overestimated. This deviation also increased for standard deviation σ . For the more narrow distribution of $\sigma \leq 0.3$, the overestimation was limited to percentages $\leq 10\%$. But for deviations $\sigma = 0.4$ they were closer to $\sim 20\%$.

EXPERIMENTAL APPLICATION:

To test our thermomagnetic model we investigated composite MnAs-GaAs films ranging from 20-50 nm thick that were grown via molecular beam epitaxy (MBE). These films were created by first growing a homogenous film of $Ga_{1-x}Mn_xAs$, $x = 0.1$ at 250 °C, then exposing it to a subsequent thermal anneal. The annealing parameters can be adjusted to produce varying magnetic properties and distributed superparamagnetic MnAs nanoparticles in the GaAs lattice. The particles range from small superparamagnetic nanodots to larger single-domain ferromagnets. Figure 10 shows the effect that annealing the films has on their magnetic properties.^{44,45,46}

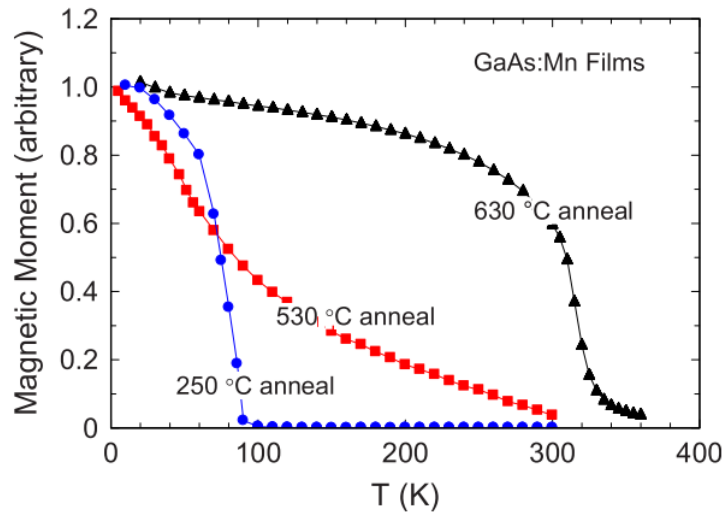


Figure 10: magnetic moment of GaAs:Mn vs temperature for 7% Mn. Annealed samples: (i) 250 °C air annealed homogeneous $Ga_{0.93}Mn_{0.07}As$ with $T_c=90$ K (circles); (ii) 530 °C annealed superparamagnetic MnAs nanoparticles in GaAs matrix (squares); and (iii) 630 °C annealed ferromagnetic MnAs nanoparticles in GaAs (triangles).

These magnetic properties were measured with a SQUID magnetometer from Quantum Design with the applied field oriented in the plane of the films. The physical size distribution was obtained by manually analyzing SEM micrographs taken throughout the surface of the samples (as seen in the inset of Figure 11). The actual crystal structure of the particles has not been determined, but typically slow annealing like this produces a zincblende or NiAs-type hexagonal structure^{47,48,49,50}.

The $m_{ZFC}(T)$ data shown in Figure 11 was obtained by first cooling the sample to low temperature. Then a small field of 50-100 Oe is applied and the sample is heated back up to higher temperatures. The data for both anneals shows a blocking temperature followed by a $1/T$ paramagnetic dependence for increasing temperature. The maximum (T_B , aka blocking temperature) for the sample annealed at 580 °C lies at a higher temperature than that for the sample that was annealed at 530 °C; corresponding to a larger particle size.

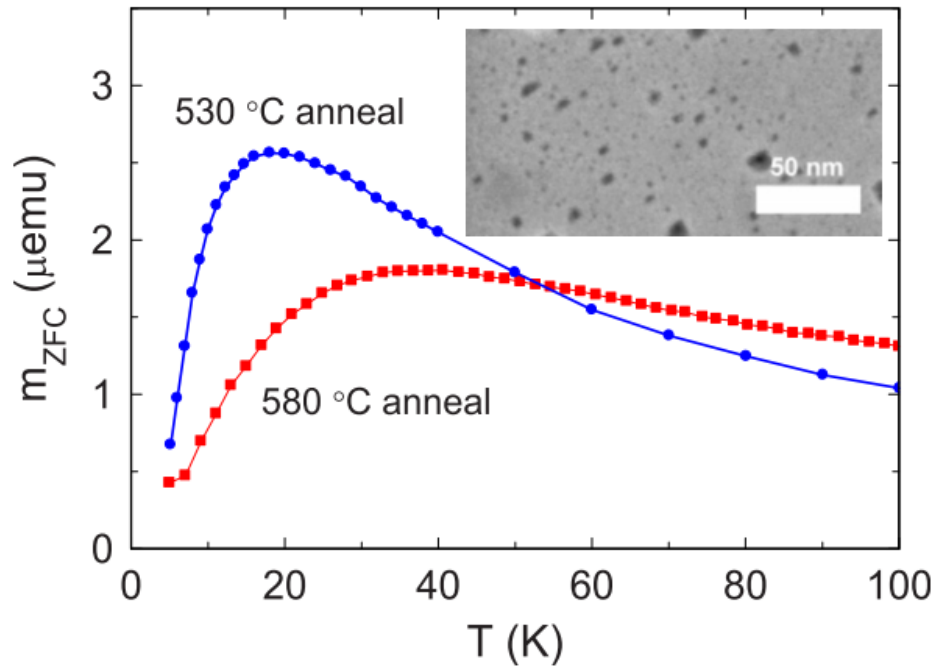


Figure 11: Magnetic moment vs. temperature for films containing MnAs nanoparticles in GaAs matrix. The zero-field cooling data for a film annealed at 530° C for 30min is shown by the circles (squares). The inset shows a SEM micrograph of MnAs nanoparticles for the film annealed at 530 °C, where the bar represents 50 nm.

From this data the model can be applied to find the distribution of particle diameters. First, the distribution of blocking temperatures $f(T_B)$ for the two samples from Figure 11 were computed from equation (3). Next, the thermomagnetic distribution of diameters $f(D)$ was computed from $f(T_B)$ via equation (1) with $V = \frac{\pi D^3}{6}$.

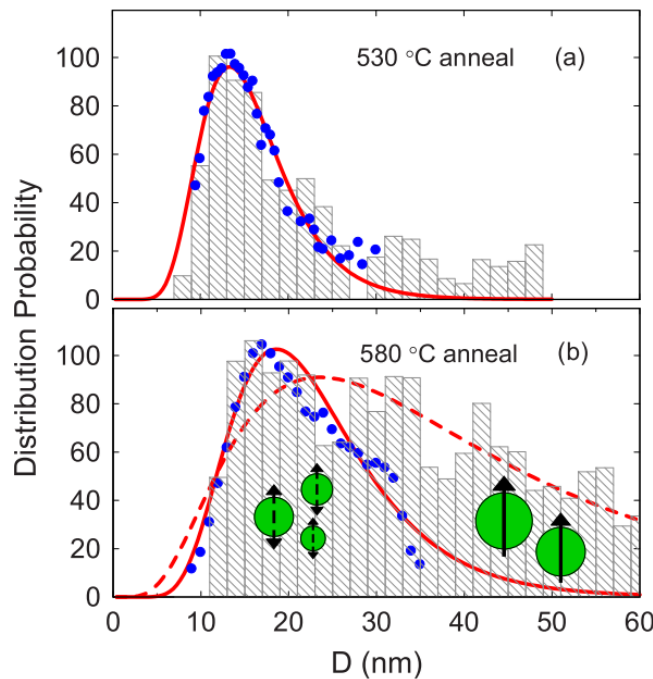


Figure 12: Distribution probability vs. particle diameter, $f(D)$, for MnAs nanoparticles in GaAs matrix films. Solid data points represent diameters derived from thermomagnetic analysis of the ZFC moment using Eq. 3. The histograms represent the physical diameters obtained from electron microscopy. The solid curves are the fits of a log-normal function to the thermomagnetic data. (a) Data for the film annealed at 530 °C has a median particle diameter of 15.0 nm and standard deviation $\sigma=0.34$. (b) Data for the film annealed at 580 °C, where the dashed curve is a log-normal fit to the histogram. The small (large) round objects represent magnetic nanoparticles with fluctuating (static) moments.

Figure 12 compares the computed $f(D)$ on a plot of particle diameter vs. distribution probability for both the annealed samples from Figure 11. It also shows the histograms for both the samples manually obtained from the SEM micrographs. The thermomagnetic distribution plot was made to overlap the histogram by choosing a value for the effective uniaxial anisotropy constant K_{eff} . For both films $K_{eff} = 4 \times 10^4 \text{ erg/cm}^3$ was used. It is important to note that the value for K_{eff} simply sets the **scale** of the D axis. As a result, the width of the log-normal distribution given in the equation by σ is **independent** of the value of K_{eff} . This is why we can determine an estimate for the K_{eff} by plugging in different values until the thermomagnetic distribution overlaps the fit for the manually determined histogram. Figure 12a shows excellent agreement between the modeled diameters (solid dots) and the histogram of particle diameters measured manually. It even shows a slow decrease in particle sizes on the large particle diameter side of the peak, which is also characteristic of a log-normal distribution. The solid curve in the graph is a fit to the solid dots (thermomagnetic data) using a log-normal function

with a mean particle diameter of $D = 15.9 \text{ nm}$ and a standard deviation of $\sigma = 0.34$.

Contrasting the well-fit data of the sample annealed at $530 \text{ }^\circ\text{C}$ is the plot for the sample annealed at $580 \text{ }^\circ\text{C}$ in Figure 12b. this shows a large difference on the large diameter side of the graph between the modeled thermomagnetic distribution and the manually obtained histogram. This difference is evident by comparing the log-normal fit to the thermomagnetic data (solid line) with the log-normal fit to the histogram data (dashed line). The thermomagnetic distributions' accuracy is confined to the area of small diameters. This is expected since the larger particles (which there are many of in this sample) exceed the superparamagnetic limit (diameter for superparamagnetism to occur) and therefore do not contribute to the ZFC thermal blocking behavior. Thus, superparamagnetism is limited to 30-40 nm for this system.

Finally, we discuss the anisotropy constant found in this study. By adjusting K_{eff} to alter the D-axis scale in Figure 12a to align with the log-normal fit for the thermomagnetic data, we determined $K_{eff} \approx 4 \times 10^4$. This anisotropy constant associated with our embedded MnAs nanocrystals is much smaller than expected based on previous studies. The table below shows previously measure anisotropy constants for MnAs bulk⁵¹, MnAs on GaAs thin films^{52,53,54,55}, and nanocrystals⁵⁶ (which were somewhat smaller than this study at $D = 5\text{-}8 \text{ nm}$). The smaller anisotropy constant for these embedded MnAs nanocrystals could arise from either a modified crystal structure or electrical field effects at the particle-matrix interface. Further investigation could be done to probe possible crystal modifications such as a particle-to-matrix, matrix-to-substrate, or interfacial lattice mismatch induced strain.

<u>Magnetocrystalline Anisotropy Constants (K_{eff}) for MnAs</u>	
BULK:	$76 \times 10^4 \text{ erg/cm}^3$
THIN FILMS ON GaAs:	$12 \times 10^4 - 72 \times 10^4 \text{ erg/cm}^3$
NANOCRYSTALS 5-8nm dia.:	$14 \times 10^4 - 18 \times 10^4 \text{ erg/cm}^3$

CONCLUSION:

Here it is shown that thermomagnetic data obtained from an ensemble of superparamagnetic nanoparticles can be transformed into a distribution of particle sizes. Furthermore this distribution can be fit to a log-normal curve. In addition to the size distribution, the nanocrystals' anisotropy constant, K_{eff} , can be determined by combining the thermomagnetic distribution with the physical size distribution found via SEM imaging. In doing this it was found that the MnAs anisotropy constant is significantly modified for nanometer size particles within a GaAs matrix. Most importantly this technique is a non-invasive method for characterizing the size distribution of superparamagnetic nanoparticles that can be applied to a vast array of magnetic nanomaterials in many areas of study.

Bibliography:

- ¹ S.P. Bennett, L. Menon, and D. Heiman, "Magnetic Properties of GaMnAs Nanodot Arrays Fabricated using Porous Alumina Templates", *J. Appl. Phys.* **104**, 024309 (2008).
- ² H.G. Johnson, S.P. Bennett, R. Barua, L.H Lewis, and D. Heiman, "Universal Properties of Linear Magnetoresistance in Strongly Disordered Semiconductors", *Phys. Rev. B* **82**, 085202 (2010).
- ³ R.S. DiPietro, H.G. Johnson, S.P. Bennett, T. Nummy, L.H Lewis, and D. Heiman, "Determining magnetic nanoparticle size distributions from thermomagnetic measurements", *Appl. Phys. Lett.* **96**, 222506 (2010).
- ⁴ C.P. Bean, J.D. Livingston, *J. Appl. Phys.* **30** (1959) 120S.
- ⁵ Ekimov, A. I. & Onushchenko, A. A. (1981) "Quantum size effect in three-dimensional microscopic semiconductor crystals". *JETP Lett.* **34**: 345–349. Bibcode 1981JETPL..34..345E.
- ⁶ S. Sun, C.B. Murray, D. Weller, L. Folks, A. Moser, *Science* **287** (2000) 1989.
- ⁷ R.P. Cowburn, M.E. Welland, *Science* **287** (2000) 1466.
- ⁸ R.P. Cowburn, *Phys. Rev. B* **65** (2000) 092409.
- ⁹ R. Hanson, L.P Kouwenhoven, J. R. Petta, S. Tarucha, and L. M. K. Vandersypen, *Rev. Mod. Phys.* **79**, 1217 (2007); see also arXiv:cond-mat/0610433.
- ¹⁰ R. P. Cowburn, *J. Magn. Mater.* 242-245, **505** (2002).
- ¹¹ M. A. Willard, L. Kurihara, E. E. Carpenter, S. Calvin, and V. G. Harris, *Int. Mater. Rev.* **49**, 125 (2004).
- ¹² *Encyclopedia of Nanoscience and Nanotechnology* (American Scientific, Stevenson Ranch, CA, 2004), Vol. **1**, pp.815-848.
- ¹³ B. D. Terris and T. Thomson, *J. Phys. D* **38** R199 (2005).
- ¹⁴ A. I. Ekimov, A. A. Onushchenko, *Sov. Phys. Semicon.* **775** (1982).
- ¹⁵ <http://www.grin.com/en/doc/278572/hydrogen-in-ferromagnetic-semiconductors-for-planar-spintronics>.
- ¹⁶ H. Masuda, K. Yasui, and K. Nishio, *Adv. Mater. (Weinheim, Ger.)* **12**, 1031 (2000).
- ¹⁷ C. -P. Li, I. V. Roshchin, X. Battle, M. Viret, F. Ott, and I. K. Schuller, *J. Appl. Phys.* **100**, 074318 (2006).
- ¹⁸ J. Liang, H. Chik, A. Yin, and J. Xu, *J. Appl. Phys.* **91**, 2544 (2002).
- ¹⁹ H. Masuda, M. Wantanabe, K. Yasui, D. Tryk, T. Rao, and A. Fujishima, *Adv. Mater. (Weinheim, Ger.)* **12**, 444 (2000).
- ²⁰ H. Hu, and D. He, *Mater. Lett.* **60**, 1019 (2006).
- ²¹ K. Yasui, K. Nishio, H. Nunokawa, and H. Masuda, *J. Vac. Sci. Techno. B* **23**, L9 (2005).
- ²² H. Masuda and K. Fukuda, *Science* **268**, 1466 (1995).
- ²³ H. Masuda, H. Yamada, M. Satoh, H. Asoh, M. Nakao, and T. Tamamura, *Appl. Phys. Lett.* **71**, 2770 (1997).
- ²⁴ K. C. Ku, S. J. Potashnik, R.F. Wang, S. H. Chun, P. Schiffer, N. Samarth, M. J. Seong, A. Mascarenhas, E. Johnston-Halperin, R. C. Myers, A. C. Gossard, and D. D. Awschalom, *Appl. Phys. Lett.* **82**, 2302 (2003).
- ²⁵ K. Edmunds, P. boguslawski, K. Wang, R. Champion, S. Novikov, N. Farley, B. Gallagher, C. Foxon, M. Sawicki, T. Dietl, M. Nardelli, and J. Bernhole, *Phys. Rev. Lett.* **92**, 037201 (2004).
- ²⁶ E. C. Stoner and E. P. Wohlfarth, *Philos. Trans. R. Soc. London, Ser. A* 240, 599 (1948); *IEEE Trans Magn.* **27**, 3475 (1991).
- ²⁷ A. Aharoni, *Introduction to the Theory of Ferromagnetism* (Oxford Science, New York, 2000).
- ²⁸ C. Gould, K. Pappert, G. Schmidt, and L. W. Molenkamp, *Adv. Mater (Weinheim, Ger.)* **19**, 323 (2007).

- ²⁹ M. Sawicki, K.-Y. Wang, K. W. Edmonds, R. P. Champion, C. R. Staddon, N. R. S. Farley, C. T. Foxon, E. Papis, E. Kamioska, A. Piotrowska, T. Dietl, and B. L. Gallagher, *Phys. Rev. B* **71**, 121302 (2005).
- ³⁰ R. Xiu, A. Husmann, T. F. Rosenbaum, M.-L. Saboungi, J. E. Enderby, and P. B. Littlewood, *Nature (London)* **390**, **57** (1997).
- ³¹ S. L. Bud'ko, P. C. Canfield, C. H. Mielke, and A. H. Lacerda, *Phys. Rev. B* **57**, 13624 (1998).
- ³² A. Husmann, J. B. Betts, G. S. Boebinger, A. Migliori, T. F. Rosenbaum, and M.-L. Saboungi, *Nature (London)* **417**, 421 (2002).
- ³³ J. Hu and T. F. Rosenbaum, *Nature Mater.* **7**, 697 (2008).
- ³⁴ H. Ohno, A. Shen, F. Matsukura, A. Oiwa, A. Endo, S. Katsumoto, and Y. Iye, *Appl. Phys. Lett.* **69**, 363 (1996).
- ³⁵ J. De Boeck, R. Oesterholt, A. Van Esche, H. Bender, C. Bruynseraede, C. Van Hoof, and G. Borghs, *Appl. Phys. Lett.* **68**, 2744 (1996).
- ³⁶ (B. Lakshmi, G. Favrot, and D. Heiman, *Proc. SPIE* 5359, 290 (2004).
- ³⁷ M. von Kreutzbruck, G. Lembke, B. Mogwitz, C. Korte, and J. Janek, *Phys. Rev. B* **79**, 035204 (2009).
- ³⁸ M. M. Parish and P. B. Littlewood, *Phys. Rev. B* **72**, 094417 (2005).
- ³⁹ J. Hu, M. M. Parish, and T. F. Rosenbaum, *Phys. Rev. B* **75**, 214203 (2007).
- ⁴⁰ M. von Kreutzbruck, G. Lembke, B. mogwitz, C. Korte, and J. Janek, *Phys. Rev. B* **79**, 035204 (2009).
- ⁴¹ C. Kittel, *Introduction to Solid State Physics*, Wiley, New York, (2005).
- ⁴² J. Hu, M. M. Parish, and T. F. Rosenbaum, *Phys. Rev. B* **75**, 214203 (2007).
- ⁴³ M. El-Hilo, K. O'Grady, and R. W. Chantrell, *J. Magn. Magn. Mater.* **114**, 295 (1992).
- ⁴⁴ J. De Boeck, R. Oersterholt, A. Van Esch, H. Bender, C. Bruynseraede, C. Van Hoof, and G. Borghs, *Appl. Phys. Lett.* **68**, 2744 (1996).
- ⁴⁵ M. Moreno, A. Trampert, B. Jenichen, L. Däwertz, and K. H. Ploog, *J. Appl. Phys.* **92**, 4672 (2002).
- ⁴⁶ A. Kwaitkowski, D. Wasik, M. Kamińska, R. Bożek, J. Szczytko, A. Twardowski, J. borysiuk, J. Sadowski, and J. Gosk, *J. Appl. Phys.* **101**, 113912 (2007).
- ⁴⁷ J. De Boeck, R. Oersterholt, A. Van Esch, H. Bender, C. Bruynseraede, C. Van Hoof, and G. Borghs, *Appl. Phys. Lett.* **68**, 2744 (1996).
- ⁴⁸ M. Moreno, A. Trampert, B. Jenichen, L. Däwertz, and K. H. Ploog, *J. Appl. Phys.* **92**, 4672 (2002).
- ⁴⁹ A. Kwaitkowski, D. Wasik, M. Kamińska, R. Bożek, J. Szczytko, A. Twardowski, J. borysiuk, J. Sadowski, and J. Gosk, *J. Appl. Phys.* **101**, 113912 (2007).
- ⁵⁰ M. Yokoyama, H. Yamaguchi, T. Ogawa, and M. Tanaka, *J. Appl. Phys.* **97**, 10D317 (2005).
- ⁵¹ R. W. De Blois and D. S. Rodbell, *Phys. Rev.* **130**, 1347 (1963).
- ⁵² J. Lindner, T. Tolinski, K. Lenz, E. Kosubek, H. Wende, K. Baberschke, A. Ney, T. hesjedal, C. Pampuch, R. Koch, L. Däwertitz, and K. H. Ploog, *J. Magn. Magn. Mater.* **277**, 159 (2004).
- ⁵³ A. H. V. Repetto Llamazares, J. Milano, L. B. Steren. V. Garcia, M. Marangolo, M. Eddrief, and V. H. Etgens, *Physica B* **398**, 372 (2007).
- ⁵⁴ F. Schippan, G. Behme, L. Daweritz, K. H. Ploog, B. Dennis, K.-U. Neumann, and K. R. A. Ziebeck, *J. Appl. Phys.* **99**, 2766 (2000).
- ⁵⁵ G. E. Sterbinsky, S. J. May, P. T. Chiu, and B. W. Wessels, *Physica B* **388**, 370 (2007).
- ⁵⁶ A. Kwiatkowski, D. Wasika, P. Dluzewski, J. Borysiuka, M. Kaminska, A. Twardowski, and J. Sadowski, *J. Magn. Magn. Mater.* **321**, 2788 (2009).